Stem Cell Research & Therapy

RESEARCH Open Access

FTO-mediated m6A modification regulates the osteogenic differentiation of ADSCs by targeting FOXO1

Zhaohua Wang[1,2†], Si Wen[3†], Huizheng Li[2], Xiaosu Wang[1], Shu Guo[1*] and Shude Yang[1*]

Abstract

Using adipose-derived stem cells (ADSCs) has recently become a crucial approach for treating bone defects owing to their ease of accessibility and substantial differentiation potential. N6-methyladenosine (m6A) modification greatly influences biological processes and determines the differentiation fate of stem cells. However, the specific mechanisms by which m6A modification influences the osteogenic differentiation of ADSCs remain unclear. We identified FOXO1 as the key m6A-modified gene during the osteogenesis of ADSCs. Furthermore, demethylase FTO enhanced RUNX2 expression while inhibiting PPARG expression by modifying FOXO1, thereby facilitating ADSC osteogenesis. FTO knockdown inhibited ADSC migration and proliferation and impaired osteogenesis by suppressing FOXO1. At the mechanistic level, we first revealed that FTO was exported to the cytoplasm and then directly bound with FOXO1 mRNA at its 1760th bp site. Consistent use of non-steroidal anti-inflammatory drugs (NSAIDs) containing FTO inhibitors impeded ADSC-mediated bone formation both in vivo and in vitro. In summary, our study reveals the role of m6A modification based on the FTO–FOXO1–RUNX2/PPARG axis in regulating the osteogenic differentiation of ADSCs, thereby improving the clinical use of ADSCs and providing strategies for related drug applications in bone regeneration.

Keywords Adipose-derived stem cells, Osteogenic differentiation, M6A, FOXO1, FTO

Introduction

Bone defects are caused by trauma, tumors, infections, congenital deformities and the exacerbation of related diseases. Over 6 million patients suffer from bone defects annually in China [1]. Owing to the limited regenerative capacity of bone tissue, defects over the critical size often result in delayed or even nonunion fractures. Traditional transplantation material, including autogenous, allograft, and synthetic bone substitutes, exhibits certain limitations, such as donor site defects, poor bone quality, and confined applicability of graft materials. The latest bone tissue engineering concept combines biomaterials with cells or healing factors to promote bone regeneration [2]. Stem cell therapy, an important branch of regenerative

†Zhaohua Wang and Si Wen have contributed equally to this work.

*Correspondence:
Shu Guo
sguo@cmu.edu.cn
Shude Yang
sdyang@cmu.edu.cn
[1]Department of Plastic Surgery, The First Hospital of China Medical University, Shenyang 110001, Liaoning, China
[2]Department of Otorhinolaryngology & Head and Neck Surgery, Dalian Municipal Friendship Hospital, Dalian 116000, Liaoning, China
[3]Department of Nephrology, The First Affiliated Hospital of Dalian Medical University, Dalian 116000, Liaoning, China

medicine, provides a new option for patients who are unfit for traditional treatments.

Mesenchymal stem cells (MSCs) are a common type of somatic stem cells known for their self-renewal and differentiation abilities. They are primarily derived from bone marrow, adipose tissue, and umbilical cord [3]. Compared with bone marrow mesenchymal stem cells (BMSCs), ADSCs are better suited for bone tissue regeneration. Bone marrow aspiration is challenging, and BMSCs are uncommon, constituting less than 0.01% of monocytes [4].Compared with BMSCs, ADSCs are more readily available and abundant. Additionally, ADSCs demonstrate (1) similar or even higher regenerative capacity; (2) higher proliferative activity; (3) greater secreted regeneration factors; (4) immunosuppressive ability [5]. To stimulate angiogenesis and osteogenesis, ADSCs release a variety of peptides, hormones, and growth factors. They also produce chemokines to recruit endogenous stem cells to bone defect sites [6].

Epigenetic regulation of gene expression is critical to cellular function, as it controls the synthesis of proteins and modulatory molecules. In eukaryotes, DNA is tightly compacted into chromatin, limiting transcriptional machinery access. However, epigenetic modifications, including DNA methylation, histone modifications, and non-coding RNAs, can induce heritable changes in gene expression by altering chromatin structure and accessibility [7]. These processes extensively influence cell phenotype and function, which is crucial for MSC fate determination, differentiation, and functional specialization, with broad implications for stem cell biology and regenerative medicine [8]. Over 80% of all RNA methylation occurs by m6A modification (via methyltransferases, demethylases, and binding proteins), with approximately 25% of mRNAs containing at least one m6A [9, 10]. The alteration is essential for stem cells to differentiate into specific lineages, particularly as a decisive "switch." However, the role of m6A modification in key genes involved in the osteogenic differentiation of ADSCs remains unclear [11–13]. Therefore, this study aimed to highlight the important regulatory mechanism of m6A in the osteogenic differentiation of ADSCs mediated by FTO and verify the role of the FTO–FOXO1–RUNX2/PPARG axis in this biological process, thus providing specific guidance for the application of relevant clinical drugs on osteogenic differentiation. This offers a potential strategy for bone tissue engineering and regeneration based on ADSCs.

Methods

Isolation of ADSCs

ADSCs collection was approved by the Ethics Committee of the First Hospital of China Medical University (February 26, 2018, [2018]2018-110-2). All ADSCs were obtained from discarded adipose tissue of patients who underwent abdominal liposuction. Adipose tissue was added to centrifuge tubes and washed with sterile phosphate-buffered saline (PBS; Biosharp, China). Subsequently, the samples were centrifuged at 1000 *g* for 5 min to remove blood cells and tissue debris. This was repeated 3–5 times before digestion using 0.2% collagenase type I (Sigma, USA) at 37 ℃ for 60 min. To neutralize enzyme activity, MEM Alpha (Gibco, USA) containing 10% fetal bovine serum (FBS; Gibco, USA) was added to the digested lipoaspirates for 5 min and centrifuged at 1000 *g* for 5 min. Finally, the cells were plated in dishes and cultured with proliferation medium (MEM Alpha, 10% FBS, and 1% penicillin-streptomycin solution) at 37 ℃ in 5% CO2 with saturated humidity. ADSCs were dissociated and passaged by using 0.25% trypsin-EDTA (Gibco, USA). ADSCs at passages 3–5 were used for subsequent experiments. When the cell attachment rate was about 90%, the cells were cultured in groups with proliferation medium or complete osteogenic differentiation medium (ADHX-D101R, HyCyte™, China).

Flow cytometric analysis

ADSCs were digested with trypsin to form a single-cell suspension solution. The cells were resuspended with 500 μL binding buffer and incubated (at 37 ℃ in the dark for 45 min) with CD73, CD90, CD34, CD79a, CD14, CD45, and CD19 (Abcam, USA), as well as IgG (Proteintech, China) in each group. The results were analyzed using flow cytometry (LSR II, BD Biosciences, USA) and FlowJo software (Version 10.0).

Alizarin red S (ARS) staining and calcium quantification

The culture dish medium was removed. After that, 500 μL of 4% paraformaldehyde (Biosharp, China) was added to each dish and incubated at room temperature for 30 min to fix ADSCs. After fixation, the dish was rinsed with PBS and stained with 1 mL of 1% ARS (pH 4.2) (Solarbio, China) for 30 min. The central field view was photographed. For ARS quantification, 10% cetylpyridinium chloride monohydrate (Rhawn, China) was used to destain cells for 1 h at room temperature. Subsequently, 200 μL of eluent was transferred into a 96-well plate, and the spectrophotometric absorbance was measured at 562 nm.

Alkaline phosphatase (ALP) staining and quantification

ADSCs were fixed in 4% paraformaldehyde for 30 min. Second, the ALP staining solution was prepared according to the instructions of the Alkaline Phosphatase Color Development Kit (Beyotime, China). The cells were stained at 37 ℃ in the dark for 2 h. The central field of view of the dish was photographed using a microscope.

Quantification of ALP activity was performed and computed with ImageJ.

m6A Dot blot

TRIzol reagent was used to extract total RNA. Isolated RNA was denatured by heating at 95 ℃ for 5 min to disrupt the secondary structure and immediately placed on ice for 5 min to prevent re-formation of the mRNA secondary structure. Total RNA samples (400/200 ng) were directly dropped onto the N + nylon membrane (GE Healthcare, USA). RNA was crosslinked with UV light at 254 nm for 5 min. After blocking, the membrane was incubated with anti-m6A antibody (Abcam, USA) overnight at 4 ℃ and washed with PBST. Subsequently, the membranes were incubated with horseradish peroxidase (HRP) secondary antibodies for 1 h and washed with PBST. Finally, the membrane was incubated with ECL substrate and visualized using the ChemiDoc Imaging System.

Gene expression omnibus (GEO) datasets source processing

The transcription profile datasets were retrieved from GEO databases. GSE37329 and GSE63754 datasets, which contain human ADSCs that differentiate into osteogenic lineage, were compared with undifferentiated cells. The microarray data of GSE37329 includes five samples (GSM916203, GSM916204, GSM916205, GSM916206, and GSM916207). The microarray data of GSE63754 includes six samples (GSM1556693, GSM1556694, GSM1556695, GSM1556696, GSM1556697, and GSM1556698). Perl software (version 5.36) was used for gene symbol annotation and merging of these two datasets. Bioconductor packages (sva and limma) and R software (version 4.1.2) were used for batch normalization. The limma package identified differential gene expression. The cutoff values were set at $p < 0.05$ and $|\log_2 FC| > 1$. Furthermore, R software was used to draw a volcano plot and heatmaps of differentially expressed genes (DEGs). Packages (colorspace, stringi, DOSE, clusterProfiler, and pathview) were used for gene ontology (GO) and Kyoto encyclopedia of genes and genomes (KEGG) enrichment analysis. STRING online database and Cytoscape (version 3.9.1) software were used to analyze and draw the protein interactions.

RNA extraction and real-time quantitative polymerase chain reaction (RT-qPCR)

Total RNA from ADSCs was extracted using TRIzol reagent (Invitrogen, USA) at days 0, 3, 7, and 14 or each time point after osteogenic induction or normal culturation. RNA concentration was measured using NanoDrop 2000 (Thermo Fisher Scientific, USA). Furthermore, RNA was reverse-transcribed into cDNA using the GoScript™ Reverse Transcription System (Promega, USA). Finally, mRNA was quantified using GoTaq qPCR Master Mix (Promega, USA) in an RT-qPCR detecting system (A6001, Bio-Rad, USA). Glyceraldehyde-3-phosphate dehydrogenase (GAPDH) was used as an internal control for mRNA. The relative RNA expression was determined using the $2-\Delta\Delta Ct$ method, and normalization was achieved with GAPDH. The sequence of relevant gene primers is as follows:

FTO-forward primer (5'-ATCTCAATGCCACCCACC AACAC-3')

FTO-reverse primer (5'-CTCCATCTTCTTCCACAG TGCTTCC-3')

FOXO1-forward primer (5'-CTGGAGGAGAGCGAG GACTTCC-3')

FOXO1-reverse primer (5'-TTGGTGATGAGGTCGG CGTAGG-3')

RUNX2-forward primer (5'-TACCACACCTACCTGC CACCAC-3')

RUNX2-reverse primer (5'-TCCATCAGCGTCAACA CCATCATTC-3')

BGLAP-forward primer (5'-CCCTCACACTCCTCGC CCTATTG-3')

BGLAP-reverse primer (5'-GGTCAGCCAACTCGTC ACAGTC-3')

COL1A1-forward primer (5'-GAACAGGGCGACAGA GGCATAAAG-3')

COL1A1-reverse primer (5'-CAACAGGACCAGCAT CACCAGTG-3')

GAPDH-forward primer (5'-AGGTCGGTGTGAACG GATTTG-3')

GAPDH-reverse primer (5'-TGTAGACCATGTAGTT GAGGTCA-3')

Dual luciferase assay

Using Lipofectamine 3000 (ThermoFisher Scientific, USA), ADSCs were transfected following the manufacturer's protocol. FOXO1 was cloned into the pcDNA3.1 vector. The WT and Mut promoter regions of RUNX2 and PPARG were inserted into the pGL3 luciferase reporter vector. To assess the binding of FOXO1 to RUNX2 and PPARG promoters, ADSCs were cultured and lysed 48 h after co-transfection with Runx2-WT/Mut or PPARG-WT/Mut. The luciferase activities of Renilla and firefly were measured using the dual luciferase reporter assay kit (Beyotime, China). All values were normalized to those of firefly luciferase and expressed as fold induction relative to basal activity.

Western blotting analysis

The proteins of ADSCs were extracted by radioimmunoprecipitation assay buffer containing 1% PMSF (Beyotime Biotechnology, China). The protein concentration was measured using a bicinchoninic acid assay kit (Abbkine,

USA). Protein samples were separated on 10% SDS-PAGE gels (Biosharp, China) and transferred to PVDF membranes (Millipore Corporation, Billerica, MA, USA). The membranes were blocked in QuickBlock™ Blocking Buffer (Beyotime, China) for 10 min at room temperature. Subsequently, the membranes were incubated with the primary antibodies overnight at 4 ℃, including FOXO1 (Proteintech, China), FTO (Proteintech, China), RUNX2 (Affinity Biosciences, China), PPARG (Proteintech, China), and GAPDH (Proteintech, China). The membranes were incubated with HRP (Elabscience, China) or LCS-HRP (Abbkine, USA) secondary antibodies for 1 h. The protein signals were detected by a chemiluminescent reagent kit (NCM Biotech, China) and visualized with a ChemiDoc Imaging System (Tanon 5200, China). Protein expressions were quantified using ImageJ Lab software.

Co-immunoprecipitation (Co-IP)

The Co-IP kit (Beyotime, China) was used according to the manufacturer's protocol. The IP lysis buffer with protease inhibitor cocktail was added to lyse the cells for 30 min. The cell lysate was incubated with FOXO1, PPARG, and IgG in a rotary mixer at 4 ℃ overnight. Protein A/G agarose gel was added and mixed at 4 ℃ for 4 h. The mixture was collected and washed with lysis buffer. The 2× SDS PAGE loading buffer was added to the samples and verified using Western blotting.

Lentivirus infection

FOXO1 short hairpin RNA (shRNA), FTO shRNA, and FOXO1-containing lentiviral particles, as well as their corresponding empty shRNA, were obtained from TsingkeBiotechnology (TsingkeBiotechnology Co., Ltd, China). The lentivirus titer was over 10^8 TU/mL. The ADSCs were infected with lentiviral particles at a multiplicity of infection of 50. After 48 h, the cells were selected with puromycin. The green fluorescent protein intensity was observed using a fluorescent inverted microscope (Olympus, Japan).

Molecular docking

The protein structures of FOXO1 (Identifier: 4lg0) and PPARG (Identifier: 1zgy) were derived from the RCSB Protein Data Bank. The HDOCK tool was used to implement protein–protein docking calculations. The ligand structures of meclofenamic acid sodium (CID 4038) and FB23-2 (CID 138454779) were acquired from PubChem. Their energies were minimized using Chembio3D software (version 14.0.0.117). The FTO protein (Identifier: 3LFM) binding pockets were identified with AutoDock Vina (version 1.1.2) and MGLTools (version 1.5.7). The molecular docking between the two ligands and the FTO protein was completed using PyMol software (version 2.5).

RNA-binding protein immunoprecipitation (RIP)

The RIP kit (BersinBio, China) was used according to the manufacturer's protocol. Using RIP lysis buffer, the ADSCs were lysed. The lysate products were incubated with magnetic beads pre-conjugated to IgG and FTO at 4 ℃ overnight. Ultimately, RNA was extracted, and FOXO1 expression level was measured by qRT–PCR.

Scratch assay

To reach confluence, ADSCs were plated into a 6-well plate and incubated. The monolayer was scratched using a tip and washed with serum-free medium to remove detached cells. Thereafter, the cells were cultured in osteogenic differentiation medium (2% FBS) and photographed at 0, 24, and 48 h later. The wound closure area was calculated as follows: migration area (%) = $(A0 - An)/A0 \times 100\%$, where A0 and An represent the initial and remaining area at the photographing point, respectively.

EdU cell proliferation assay

To detect ADSC proliferation, the EdU cell proliferation assay (Beyotime, China) was employed according to the manufacturer's instructions. About 1×10^6 cells were seeded in 6-well plates and maintained for 24 h. For cell labeling, 500 μL EdU (10 μM) reagent was added to each well and incubated for 12 h. After washing with PBS, the cells were fixed in paraformaldehyde for 15 min and permeabilized with 0.3% Triton X-100 (Biofroxx, Germany) for 15 min. ADSCs were incubated with the click-reaction reagent for 30 min at room temperature in the dark. Finally, the nucleus was counterstained with Hoechst 33,342 reagent and was observed with a fluorescence microscope system (Cytation 5, BioTek, USA).

Single-base elongation and ligation-based qPCR amplification (SELECT) detection assay

SELECT assay was performed using the Epi-SELECT™ m6A site identification kit (R202106M, Guangzhou Epibiotek Co., Ltd., China). Total RNA was extracted from ADSCs in the control and FTO knockdown groups. Reverse transcription and qPCR were performed to quantify the FOXO1 mRNA in the two groups. Following the kit instructions, RNA was mixed with up-probe, down-probe, dNTP, and reaction buffer for annealing and extension. The resulting product was mixed with a DNA polymerase, ligase, and ATP for single-base extension. The final reaction mixture, including cDNA, Select F, Select R, and qPCR master mix, was used for qPCR quantification.

Nuclear and cytoplasmic protein extraction

According to the instructions of the Nuclear and Cytoplasmic Protein Extraction Kit (PHYGENE, China),

the proliferated and osteogenic differentiated ADSCs were collected into centrifuge tubes using a cell scraper. After centrifugation, the cytoplasmic protein extraction reagent was added to lyse the cells for 10 min. The cytoplasmic protein constitutes the supernatant. Nuclear protein extraction reagent was added to lyse the rest of the cell pellets to obtain the nucleoprotein. Western blotting was performed as described above.

Cell counting kit-8 (CCK-8) assay

Cell viability was determined using the enhanced CCK-8 assay (Beyotime Biotechnology, China). Cell counting was conducted using the Countess™ 3 (Thermo Fisher, USA). Furthermore, ADSCs were seeded into 96-well plates at a density of 10,000 cells/well in 100 μL of proliferation medium and cultured at 37 ℃. After each experiment, 10 μL of CCK-8 reagent was added to each well and cultured for 72 h at 37 ℃. The optical density value was measured at 450 nm. Cell viability = [(As − Ab)/(Ac − Ab)] × 100%, where As is sample well absorbance, Ab is blank well absorbance, and Ac is control well absorbance.

RNA decay assay

After ADSCs were cultured in osteogenic differentiation medium and treated with FB23-2, 5 μg/mL actinomycin D (APExBIO, USA) was added. Total RNA at 0, 3, and 6 h was extracted, and the relative expression was detected using qPCR.

In vivo bone formation

The animal experiment was approved by the Laboratory Animal Welfare and Ethical Review of China Medical University under the title "The Application and Research of Adipose-Derived Stem Cells" with authorization number CMU20231074. Eight-week-old female BALB/c nude (nu/nu) mice ($n = 10$) were procured from SiPeiFu Biotechnology (Beijing, China). Mice were randomly grouped. To minimize potential confounders, the order of treatments and measurements, as well as the positions of animals and cages, was randomized. Hydroxyapatite/tricalcium phosphate (HA/TCP) ceramic powders (comprising 60% hydroxyapatite and 40% tricalcium phosphate) were supplied by the Medical and Bioinformatics Engineering Department of Northeastern University. HA/TCP powders (40 mg) were wetted with 100 μL proliferation medium and incubated overnight. A total of 2×10^6 ADSCs (in 200 μL proliferation medium) were mixed with the wetted HA/TCP powders and incubated at 37 ℃ overnight in 5% CO_2. Under anesthesia, a 1 cm mid-longitudinal skin incision was performed on the dorsal surface of each mouse, and a subcutaneous pocket was formed by blunt dissection. The mixture was implanted under the skin, and the incision was sutured. Overall, 10 mice were divided into two groups (control and experimental), with five mice in each group. After the third day of implantation, each mouse in the experimental group was intraperitoneally administered 2 mg/kg FB23-2 daily. Narcolan (30 μL/g) was administered intraperitoneally as anesthesia, whereas CO_2 gas was used for euthanasia. The implants were harvested at 8 weeks. The mice exhibited no visible signs of suffering throughout the experimental period. This study followed the ARRIVE guidelines 2.0.

Micro-computed tomography (micro-CT) analysis

Skyscan1276 Micro-CT (Bruker, Germany) was used to scan the implants at 55 kV, 200 μA, and 466 ms, with the filter value of 0.25 mm and pixel size of 17.520 μm. All scanned images were reconstructed using CTvox (Bruker, Germany, version 3.3) software, and the bone tissue volume (BV) of implants was determined.

Immunohistochemistry staining

The samples were paraffin sectioned and dewaxed at room temperature with 3% H_2O_2 for 5–10 min to eliminate endogenous peroxidase activity. The samples were washed with distilled water and soaked in PBS for 5 min. After blocking with 3% w/v bovine serum albumin (Boster, China) at 37 ℃ for 30 min. The slices were incubated with primary antibodies (FTO and FOXO1) overnight at 4 ℃ and subsequently incubated with secondary antibodies at 37 ℃ for 1 h. Detection was performed using 3,3'-diaminobenzidine (Beyotime, China), which precipitated a brown color on the tissue. Hematoxylin was used to stain the nucleus, which was photographed using a microscope (Leica Biosystems, USA).

Statistical analysis

The experiments in this study were independently repeated at least three times. Statistical analysis was performed by using GraphPad Prism 8.0 software, and the results were expressed as the mean ± SD. For all data, $p < 0.05$ was considered statistically significant. Statistical tests used for each experiment are listed in the figure legends.

Results

ADSCs have osteogenic differentiation potential in vitro

To obtain cells, the adipose tissue was digested with collagenase (Fig. 1A), and their specific surface markers were detected. The cells tested positive for CD73 and CD90 but negative for CD14, CD19, CD34, CD45, and CD79a (Fig. 1B). To verify their multi-differentiation potential, ADSCs were induced for osteogenic and adipogenic differentiation simultaneously for 14 days. Following osteogenic induction, the cells differentiated into osteoblasts, as evidenced by the presence of calcium nodules. Contrarily, adipogenic induction transformed the cells into

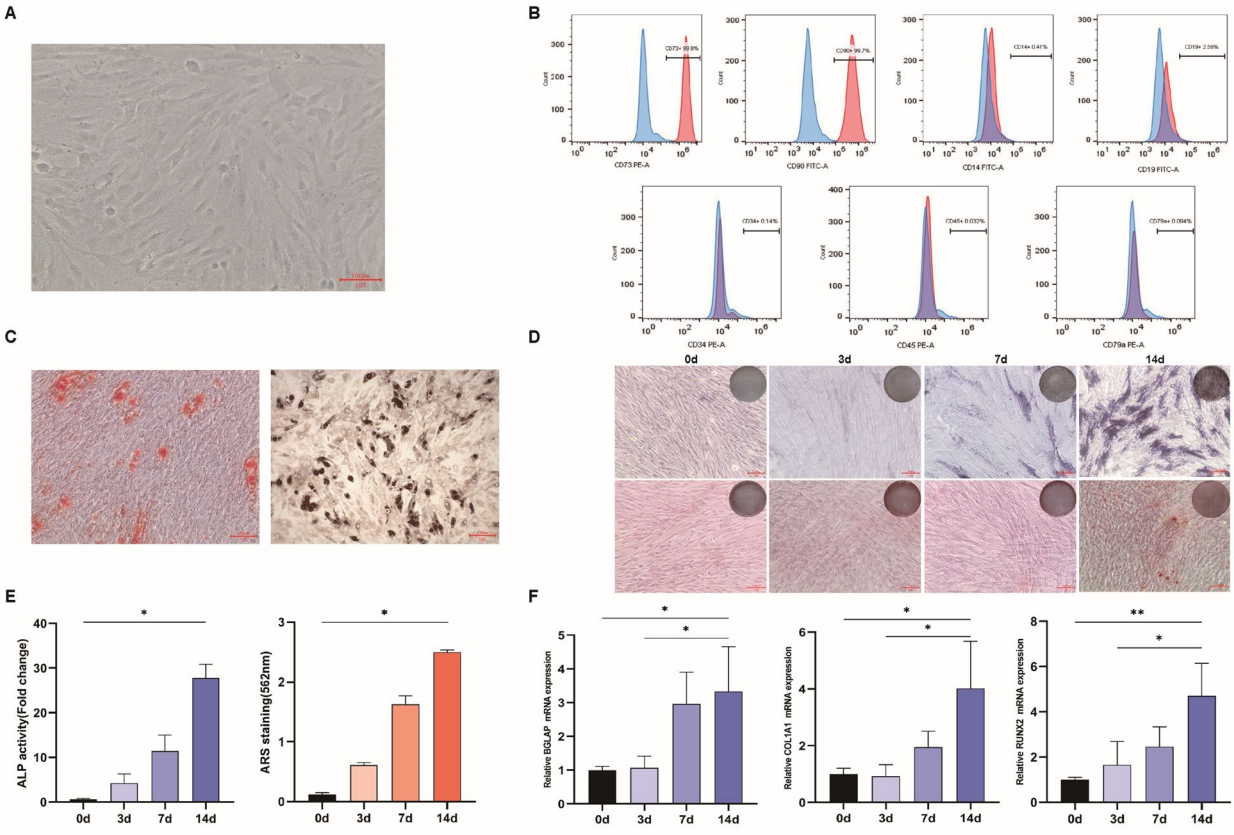

Fig. 1 ADSCs have osteogenic differentiation potential. **A** ADSCs extracted from human adipose tissues. **B** Identified surface markers of ADSCs, including CD14, CD19, CD34, CD45, CD73, CD79a, and CD90, using flow cytometry. IgG was used as an internal control. **C** Osteogenic and adipogenic differentiation potential of ADSCs. **D** Identified ADSCs cultured in osteogenic medium for 14 days using ALP and ARS staining. **E** ALP activity and ARS staining quantification of osteogenic induction. Data are presented as mean ± SD by one-way analysis of variance (ANOVA) test, $*p < 0.05$ ($n = 3$ biological replicates). **F** Detected relative mRNA expressions of the osteogenic markers BGLAP, COL1A1, and RUNX2 at different time points using qRT-PCR. Data are presented as mean ± SD using a one-way ANOVA test, $*p < 0.05$, and $**p < 0.01$ ($n = 3$ biological replicates)

adipocytes, characterized by the formation of lipid droplets after Oil Red O staining (Fig. 1C). These findings correspond with the identification standards of ADSCs. We performed ARS and ALP staining at different induction time points (days 0, 3, 7, and 14) to verify the changes in the osteogenic differentiation of ADSCs in vitro. The ALP activity of ADSCs gradually improved, accompanied by increased calcium salt deposition and calcium nodule formation (Fig. 1D). Quantitative analysis of ALP activity and ARS staining progressively enhanced the osteogenic ability of ADSCs (Fig. 1E). Moreover, the qPCR of three classic osteogenic markers (BGLAP, CO1LA1, and RUNX2) gradually increased, reaching a peak on day 14 during the osteogenesis (Fig. 1F). These outcomes revealed that the osteogenic differentiation potential of ADSCs steadily improved over time in vitro.

FOXO1 represented the potential key methylated gene in osteogenic differentiation of ADSCs

The m6A dot blot experiment confirmed m6A modifications during the osteogenic differentiation of ADSCs. Total m6A gradually increased during osteogenic differentiation and peaked on the 14th day (Fig. 2A). To clarify the key methylated gene in the osteogenic differentiation of human ADSCs, we collected the transcriptional profile datasets in the GEO database, including GSE37329 and GSE63754. Perl and R language software were used to merge and analyze the two datasets, followed by batch normalization. A total of 17,990 genes were identified during osteogenic differentiation of ADSCs. Out of 759 DEGs in both datasets, 412 genes were markedly upregulated and 347 genes were substantially downregulated (Figs. 2B, S1A). The KEGG analysis revealed that during ADSC's osteogenesis, DEGs were mainly related to the PI3K-Akt signaling pathway (Fig. 2C). Meanwhile, GO analysis demonstrated that DEGs were mainly enriched in the biological functions of glycosaminoglycan binding (Fig. 2D). To identify the protein–protein interaction (PPI) network, DEGs were analyzed with Cytoscape software (Fig. 2E). A previous study identified 182 key differentially expressed methylation genes involved in the osteogenic differentiation of ADSCs (Fig. S1B) [14]. The

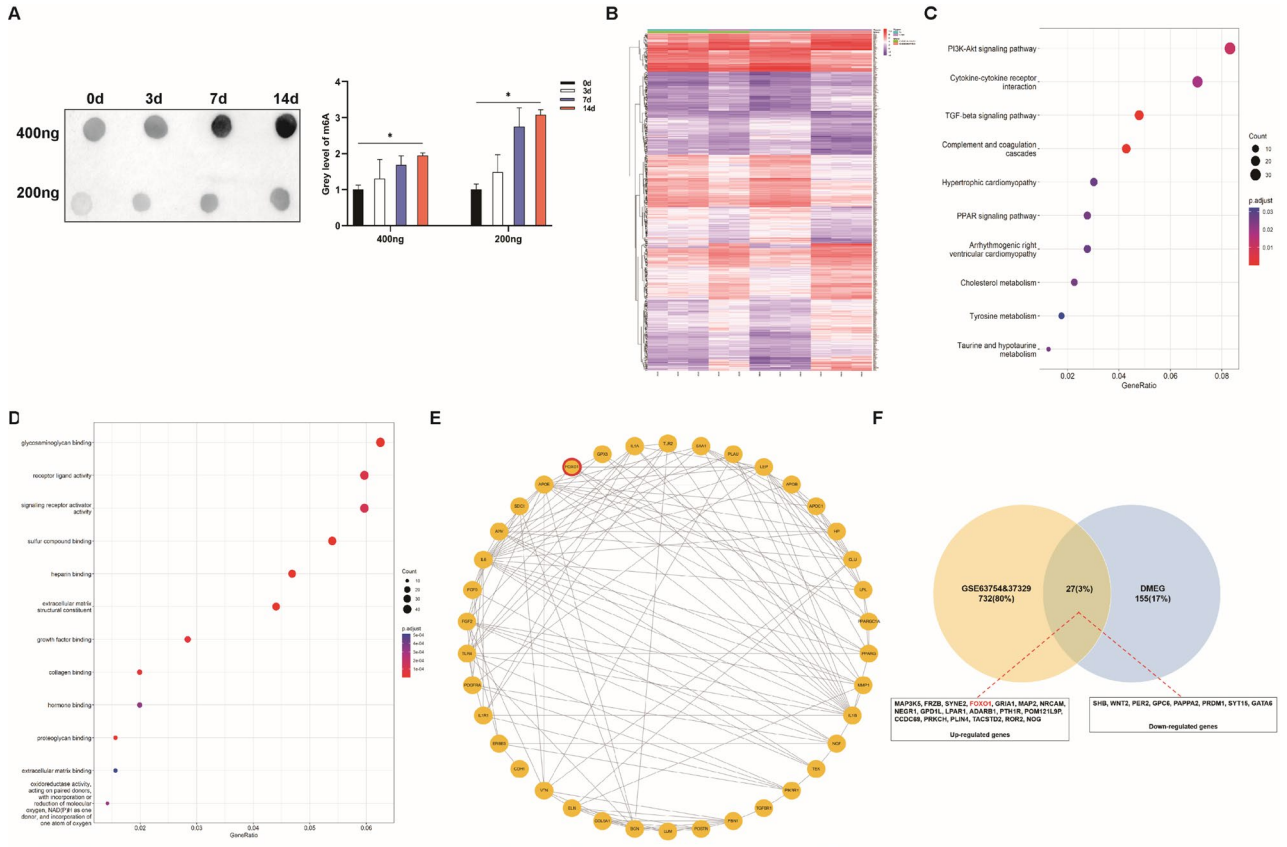

Fig. 2 FOXO1 is the potential key methylated gene associated with osteogenic differentiation of ADSCs. **A** m6A dot blots at different time points of osteogenic differentiation. Fig. S3A presents full-length blots/gels. Data are presented as mean ± SD using a two-way ANOVA test, $^{*}p < 0.05$ ($n = 3$ biological replicates). **B** Identified DEGs in GSE63754 and GSE37329 during osteogenic differentiation of ADSCs using R software. Adjusted $p < 0.05$ and $|\log_2 FC| > 1$ were set as the cutoff values. **C** DEGs enriched in relative pathways by KEGG analysis. **D** GO analyses of DEGs according to their biological functions. **E** The PPI network of DEGs revealed by Cytoscape. **F** Potential key methylated genes during osteogenic differentiation of ADSCs highlighted by a Venn diagram

Venn diagram revealed 27 key methylation genes in both datasets. Given that FOXO1 is a critical gene within the PI3K-Akt signaling pathway (Fig. S1C), plays a major role in glycosaminoglycan binding, and is a core protein of the PPI network, we assumed that FOXO1 represents the primary m6A methylated gene during ADSC's osteogenic differentiation (Fig. 2F).

FOXO1 regulated the osteogenic differentiation of ADSCs through PPARG/RUNX2

To explore the effect of FOXO1 on osteogenic differentiation of ADSCs, their expression was detected on days 0, 3, 7, and 14 of induction. The qPCR revealed that the mRNA level of FOXO1 increased with prolonged induction time, reaching a peak on day 7 (Fig. 3A). Western blotting exhibited a similar trend (Fig. 3B). Our findings were consistent with those of previous biological information analysis. Furthermore, ADSCs were initially transfected with FOXO1 lentiviral empty particles followed by lentiviral knockdown particles (Figs. S1D, E). After knocking down FOXO1, the osteogenic differentiation ability of ADSCs was drastically reduced (Fig. 3C), and quantitative analysis of ALP and ARS staining revealed a similar outcome (Fig. 3D).

RUNX2 and PPARG are classical markers of osteogenic and adipogenic differentiation in stem cells, respectively. In other cellular models, FOXO1 functioned as a transcription factor, binding to RUNX2 and PPARG promoters and regulating their transcriptional activity. Additionally, FOXO1 interacted with PPARG at the protein level (Fig. S1F) [15, 16]. We predicted potential binding sites through JASPAR and designed corresponding plasmids. The dual-luciferase assay indicated FOXO1 bound to the RUNX2 promoter to enhance its transcriptional activity, while it bound to the PPARG promoter to inhibit its transcriptional activity (Fig. 3E, F). However, no PPI was observed between FOXO1 and PPARG (Fig. S1G). FOXO1 knockdown increased PPARG and decreased RUNX2 expression in ADSCs after 14 days of osteogenic induction (Fig. 3G). This suggested that the osteogenic differentiation potential of ADSCs was decreased and their adipogenic capacity was enhanced after FOXO1 knockdown. Previous bioinformatic analysis highlighted that PPARG expression was upregulated

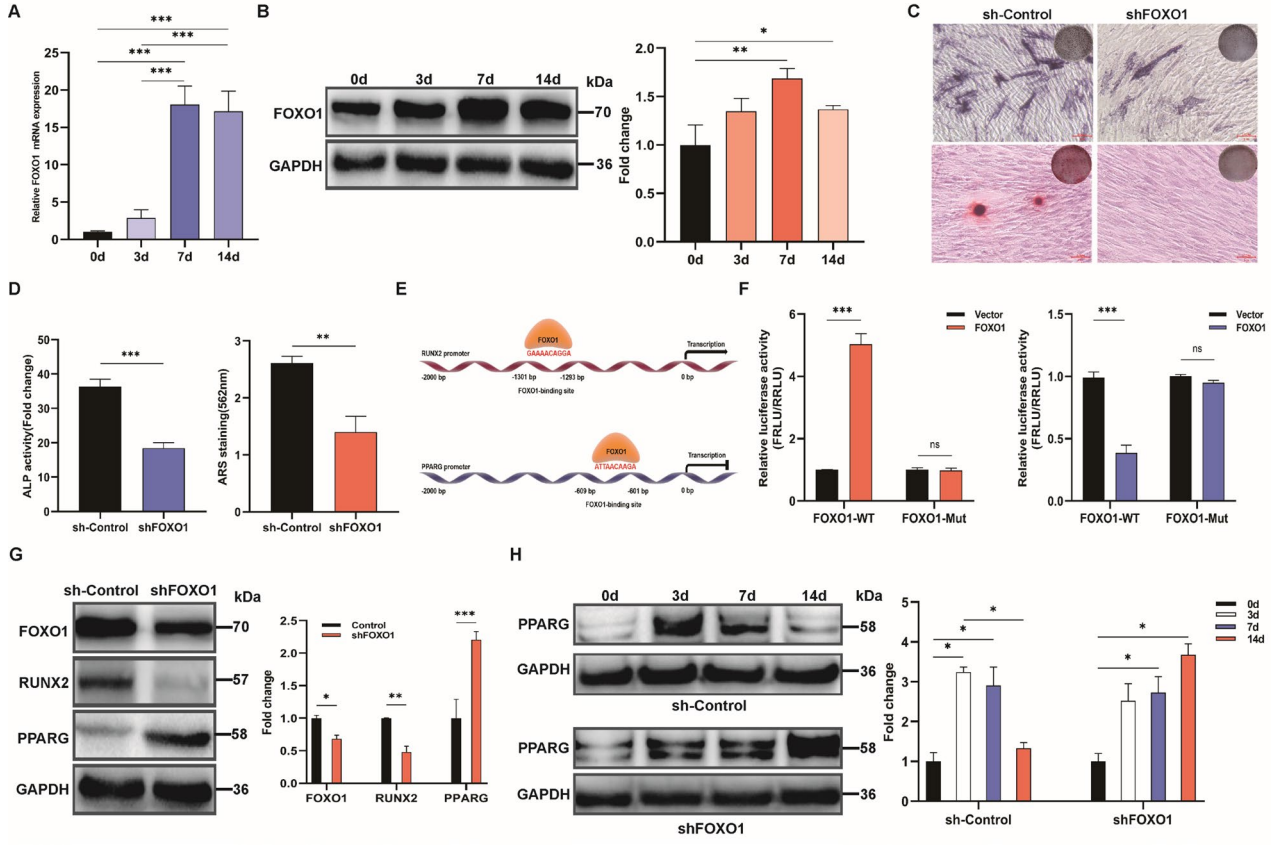

Fig. 3 FOXO1 regulates the osteogenic differentiation of ADSCs through PPARG/RUNX2. **A** Changes in FOXO1 mRNA at different time points during the osteogenic differentiation of ADSCs. Data are presented as mean ± SD; ***$p < 0.001$ ($n = 3$ biological replicates). **B** Changes in FOXO1 protein at different time points during the osteogenic differentiation of ADSCs were determined by Western blotting analysis. Fig. S3B presents the full-length blots/gels. Data are presented as mean ± SD; *$p < 0.05$ and **$p < 0.01$ ($n = 3$ biological replicates). **C** ALP and ARS staining of control and FOXO1 knockdown groups. **D** ALP activity and ARS staining quantification of control and FOXO1 knockdown groups. Data are presented as mean ± SD; **$p < 0.01$ and ***$p < 0.001$ ($n = 3$ biological replicates). **E** Specific binding sites of FOXO1 to RUNX2 and PPARG promoters. **F** Demonstration of FOXO1 as a transcription factor in regulating the transcription activity of RUNX2 and PPARG promoters using a dual-luciferase assay. Data are presented as mean ± SD by two-way ANOVA test, ***$p < 0.001$, ns: statistically non-significant ($n = 3$ biological replicates). **G** Western blotting analysis of the protein levels of FOXO1, RUNX2, and PPARG. Fig. S3C illustrates the full-length blots/gels. Data are presented as mean ± SD by two-way ANOVA test, *$p < 0.05$, **$p < 0.01$, and ***$p < 0.001$ ($n = 3$ biological replicates). **H** Changes in the protein levels of PPARG during osteogenic differentiation of ADSCs in the control and FOXO1 knockdown groups. Figs. S3D-E highlight the full-length blots/gels. Data are presented as mean ± SD by a two-way ANOVA test, *$p < 0.05$ ($n = 3$ biological replicates)

during the osteogenic differentiation (Fig. S1H). However, we observed that PPARG increased in the early stage of osteogenesis and then decreased. Nonetheless, PPARG expression continued to increase, ultimately disrupting the osteogenic differentiation (Fig. 3H).

m6A demethylase FTO targeted FOXO1 mRNA during osteogenic differentiation of ADSCs

To investigate the specific mechanism of m6A modification of FOXO1, we predicted that the FOXO1 mRNA contained multiple m6A modification sites through the SRAMP website (Fig. S2A). Four classic m6A-modifying enzymes, including FTO, ALKBH5, METTL3, and METTL14, were selected for protein-RNA docking analysis. The catRAPID suggested that FTO is the potential m6A-modifying enzyme of FOXO1 (Fig. S2B). qPCR and Western blotting indicated that the mRNA and protein levels of FTO increased with prolonged induction time and reached a peak on day 7, which was similar to that of FOXO1 (Fig. 4A, B). No visible change was observed in the mRNA or protein levels of FTO after FOXO1 knockdown, indicating that FOXO1 had no regulatory effect on FTO (Fig. 4C, D). We transfected ADSCs with FTO lentiviral empty particles and lentiviral knockdown particles (Fig.S2D, E). The qPCR revealed that FOXO1 mRNA expression decreased after FTO knockdown (Fig. 4E). Furthermore, RIP-qPCR demonstrated that FTO is targeted and enriched in FOXO1 during the osteogenic induction of ADSCs (Fig. 4F). Using a cytoplasmic and nuclear protein isolation assay, it was observed that FOXO1 expression in the cytoplasm was higher than that in the nucleus in both proliferation and osteogenic differentiation media. Nevertheless, compared with the proliferated ADSCs, FTO in the cytoplasm was higher

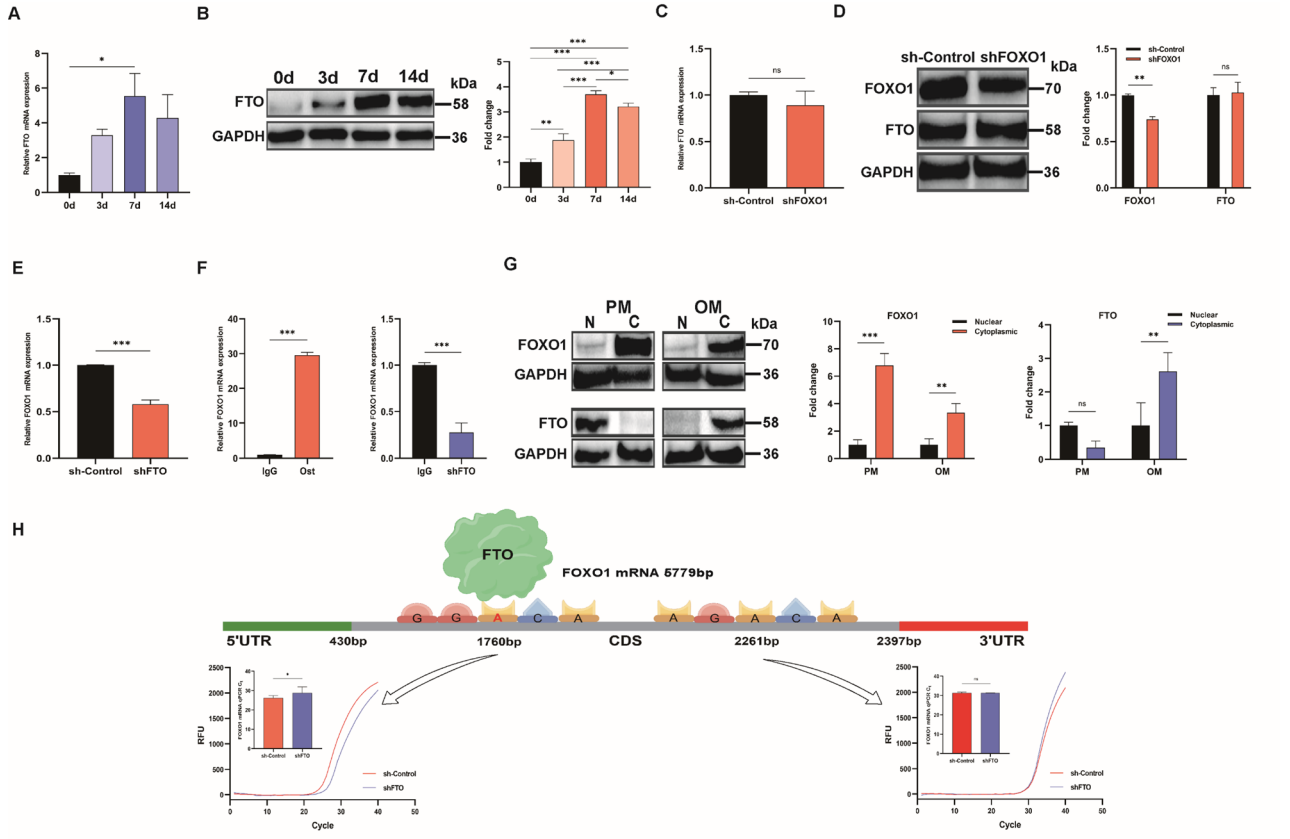

Fig. 4 Identification of FTO as the m6A demethylase of FOXO1. **A** Changes in FTO mRNA at different time points during the osteogenic differentiation of ADSCs were detected by qRT-PCR. Data are presented as ± SDs by one-way ANOVA test, $*p < 0.05$ ($n = 3$ biological replicates). **B** Changes in FTO protein during osteogenic differentiation of ADSCs determined by Western blotting analysis. Fig. S3F depicts the full-length blots/gels. Data are presented as mean ± SD by one-way ANOVA test, $*p < 0.05$, $**p < 0.01$, and $***p < 0.001$ ($n = 3$ biological replicates). **C** The mRNA level of FTO in the control and FOXO1 knockdown group was detected by qRT-PCR. Data are presented as mean ± SD by an unpaired *t*-test, ns: statistically non-significant ($n = 3$ biological replicates). **D** FTO protein level in the control and FOXO1 knockdown group was determined by Western blotting analysis. Fig. S3G presents the full-length blots/gels. Data are presented as mean ± SD by unpaired *t*-test, ns: statistically non-significant, $**p < 0.01$ ($n = 3$ biological replicates). **E** FTO knockdown reduced FOXO1 mRNA expression level. Data are presented as mean ± SD by an unpaired *t*-test, $***p < 0.001$ ($n = 3$ biological replicates). **F** RIP-qPCR detected whether FTO and FOXO1 were directly bound. Ost: osteogenesis. Data are presented as mean ± SD by an unpaired *t*-test, $***p < 0.001$ ($n = 3$ biological replicates). **G** The subcellular locations of FTO and FOXO1 were determined by cytoplasmic and nuclear protein isolation. PM: proliferation medium, OM: osteogenic medium, N: nuclear, and C: cytoplasmic. Fig. S3H presents the full-length blots/gels. Data are presented as mean ± SD by two-way ANOVA test, $**p < 0.01$, $***p < 0.001$, ns: statistically non-significant ($n = 3$ biological replicates). **H** Specific binding sites between FTO and FOXO1 by m6A-SELECT assay. Data are presented as mean ± SD by unpaired *t*-test, $*p < 0.05$, ns: statistically non-significant ($n = 7$ biological replicates)

than that in the nucleus of the osteogenic ADSCs (Fig. 4G). To further clarify the specific binding site between FTO and FOXO1, we performed the Epi-SELECT™ assay as reported previously [17]. Most m6A modifications occurred in sites of motif DRACH (D = G/A/U, R = G/A, H = A/U/C, and [G > A] m6AC [U > A > C]) and appeared around stop codons (between CDS and 3'-UTR regions) in adult human tissues [18–20]. Based on the scores and sites where FOXO1 might be m6A modified as predicted by the SRAMP website, we selected the 1760th (GG*A*CA) and 2261st (AG*A*CA) bp sites of the FOXO1 mRNA for probe synthesis and the Epi-SELECT™ assay (Fig. S2A and C). The qPCR quantification of FOXO1 in the shFTO group was reduced compared to the control group at the 1760th bp site, indicating that FTO markedly decreased the m6A level at this site in FOXO1 mRNA from osteogenic ADSCs. However, no difference was observed in FOXO1 expression at the 2261st bp site (Fig. 4H). Our findings revealed that the demethylase FTO translocated from the nucleus to the cytoplasm, where it bound to the 1760th bp site of FOXO1 mRNA and mediated m6A modification during ADSCs' osteogenesis.

FTO regulated the osteogenic differentiation of ADSCs through FOXO1

We explored the regulatory impact of FTO on the osteogenic differentiation of ADSCs. During fracture healing, MSCs migrate to the bone defect area, where they differentiate into osteoblasts and continuously proliferate to maintain bone mass [21]. When ADSCs were transfected

with FTO knockdown lentivirus, their proliferation rate substantially decreased. The scratch test revealed a notable reduction in the migration capabilities of the shFTO group at 24 and 48 h compared to the control group (Fig. 5A). Additionally, when an equal number of cells were seeded in culture dishes and subjected to an EdU experiment, the shFTO group exhibited fewer ADSCs and a considerably lower proliferation rate than the control group (Fig. 5B).

Our findings revealed that ALP staining and activity decreased following FTO knockdown. Meanwhile, ARS staining indicated lower calcium nodules in the shFTO group compared to the control group (Fig. 5C, D). Western blotting demonstrated that knocking down FTO could inhibit the FOXO1 expression and regulate PPARG and RUNX2 expression, ultimately affecting the osteogenic differentiation of ADSCs (Fig. 5E). To verify whether FOXO1 overexpression could reverse the osteogenic differentiation inhibited by FTO knockdown, ADSCs were transfected with FOXO1 overexpression particles and validated. Following 14 days of ADSC's osteogenic induction with overexpressed FOXO1, ALP, and ARS staining, along with quantitative analysis, exhibited an increased osteogenic capacity of ADSCs (Fig. 5F,

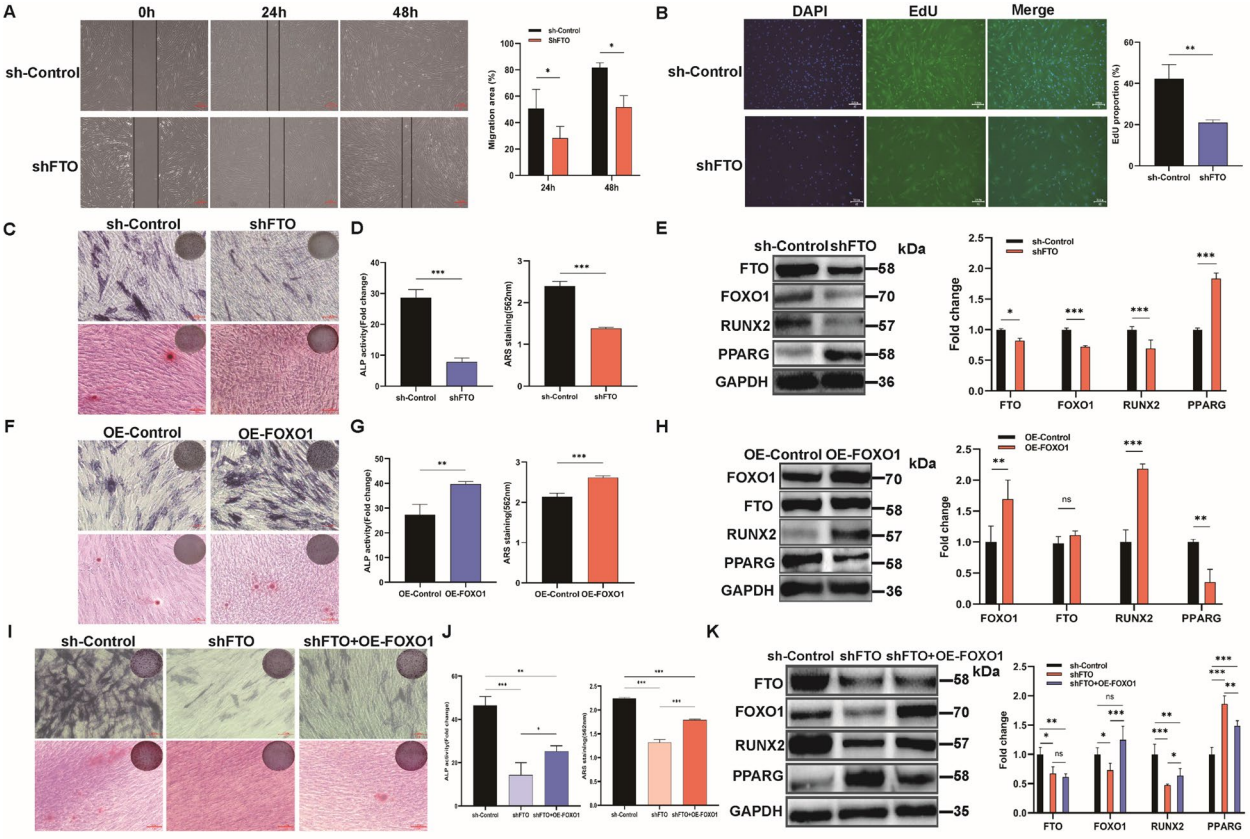

Fig. 5 FTO regulates the osteogenic differentiation of ADSCs through FOXO1. **A** Representative images of ADSC's migration determined by a scratch test at 0, 24, and 48 h. Data are presented as mean ± SD by an unpaired *t*-test, $^{*}p < 0.05$ ($n = 3$ biological replicates). **B** Representative images of ADSC's proliferation measured by EdU assay. Data are presented as mean ± SD by an unpaired *t*-test, $^{**}p < 0.01$ ($n = 3$ biological replicates). **C** ALP and ARS staining of control and FTO knockdown groups. **D** ALP activity and ARS staining quantification of the control and FTO knockdown groups. Data are presented as mean ± SD by an unpaired *t*-test, $^{***}p < 0.001$ ($n = 3$ biological replicates). **E** Protein levels of FTO, FOXO1, RUNX2, and PPARG were determined by Western blotting analysis in control and FTO knockdown groups. Fig. S4A depicts the full-length blots/gels. Data are presented as mean ± SD by two-way ANOVA test, $^{*}p < 0.05$, $^{***}p < 0.001$ ($n = 3$ biological replicates). **F** ALP and ARS staining of control and FOXO1 overexpressed groups. **G** ALP activity and ARS staining quantification of control and FOXO1 overexpressed groups. Data are presented as mean ± SD by unpaired *t*-test, $^{**}p < 0.01$, and $^{***}p < 0.001$ ($n = 3$ biological replicates). **H** Protein levels of FOXO1, FTO, RUNX2, and PPARG were determined by Western blotting analysis in control and FOXO1 overexpressed groups. Fig. S4B presents the full-length blots/gels. Data are presented as mean ± SD by two-way ANOVA test, ns: statistically non-significant, $^{**}p < 0.01$, and $^{***}p < 0.001$ ($n = 3$ biological replicates). **I** ALP and ARS staining in control, FTO knockdown, and FTO knockdown with FOXO1 overexpressed groups. **J** ALP activity and ARS staining quantification of control, FTO knockdown, and FTO knockdown with FOXO1 overexpressed groups. Data are presented as mean ± SD by one-way ANOVA test, $^{*}p < 0.05$, $^{**}p < 0.01$, and $^{***}p < 0.001$ ($n = 3$ biological replicates). **K** Protein levels of FTO, FOXO1, RUNX2, and PPARG were determined by Western blotting analysis in control, FTO knockdown, and FTO knockdown with FOXO1 overexpressed groups. Fig. S4C illustrates the full-length blots/gels. Data are presented as mean ± SD by two-way ANOVA test, $^{*}p < 0.05$, $^{**}p < 0.01$, and $^{***}p < 0.001$, ns: statistically non-significant ($n = 3$ biological replicates)

G). Western blotting revealed higher levels of FOXO1 and RUNX2 proteins, as well as lower levels of PPARG protein, in the OE-FOXO1 group compared to the OE-Control group (Fig. 5H). The sh-Control, shFTO, and shFTO + oeFOXO1 groups were induced for osteogenic differentiation for 14 days. The osteogenic ability of ADSCs in the FOXO1 overexpression group was enhanced compared to that in the shFTO group; however, it was weaker than that in the control group (Fig. 5I, J). Western blotting indicated that FOXO1 expression in the oeFOXO1 group was higher than that of the initial two groups. The PPARG expression was lower in the oeFOXO1 group than in the shFTO group but remained higher than that of the sh-Control group, whereas RUNX2 expression was higher in the oeFOXO1 group than in the shFTO group but lower than that of the sh-Control group (Fig. 5K). Summarily, FTO knockdown could impair osteogenic differentiation of ADSCs by inhibiting FOXO1, while FOXO1 overexpression could improve the osteogenic differentiation of ADSCs, partially rescuing the inhibition by FTO knockdown.

Meclofenamate sodium and FB23-2 inhibited the osteogenic differentiation of ADSCs *in vitro*

To explore the inhibitory effect of drugs or small-molecule inhibitors on the demethylase FTO, we selected meclofenamate sodium and FB23-2 as potential FTO inhibitors. Both were developed based on meclofenamic acid. The key element of their interaction group with FTO was benzylcarboxylic acid (Fig. 6A and C). We used

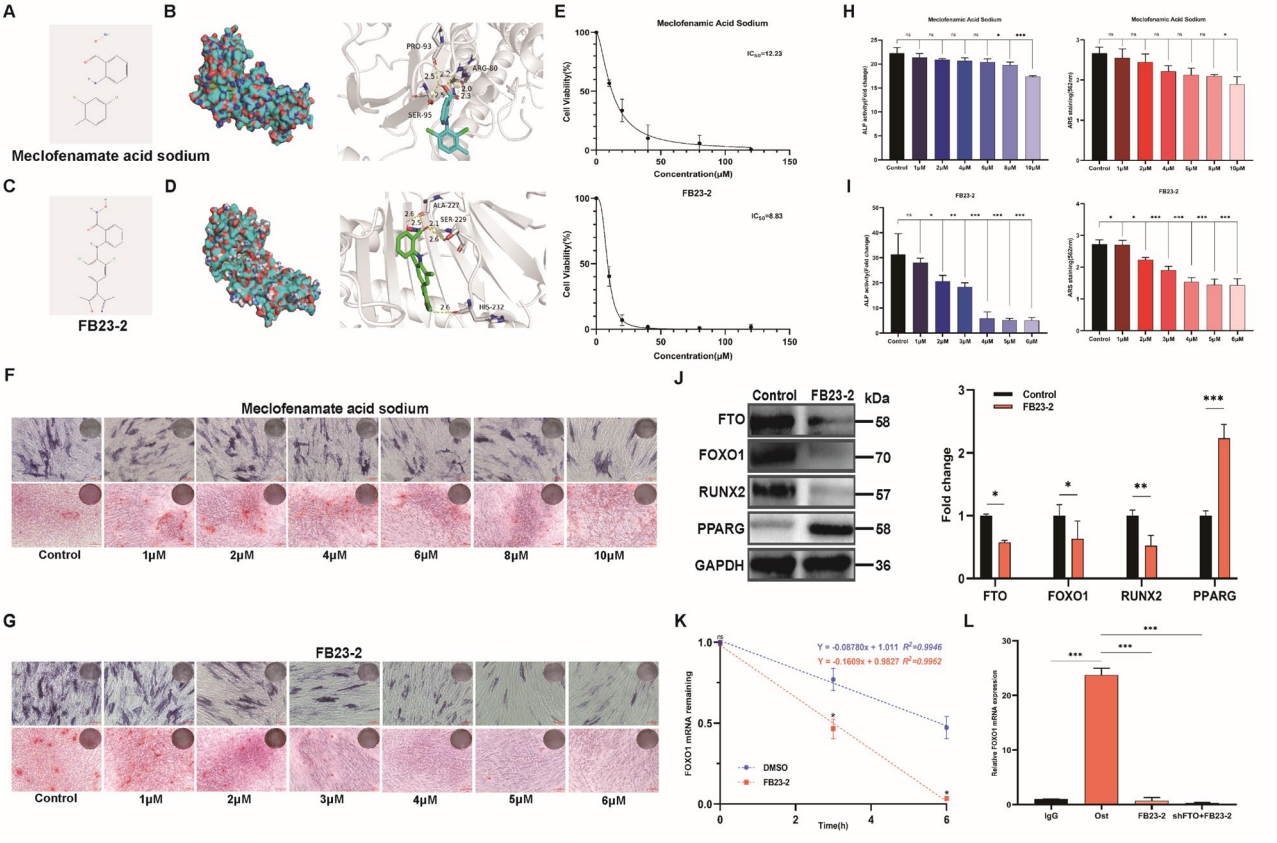

Fig. 6 FTO inhibitors impair osteogenic differentiation of ADSCs in vitro. **A** The 2D structure of meclofenamate sodium. **B** The structural complex and binding pocket of FTO with meclofenamate sodium. **C** The 2D structure of FB23-2. **D** The structural complex and binding pocket of FTO with FB23-2. **E** The IC_{50} of meclofenamate sodium and FB23-2 in ADSCs after treatment for 72 h ($n = 3$ biological replicates). **F** ALP and ARS staining were performed on osteogenesis of ADSCs treated with different concentrations of meclofenamate sodium. **G** ALP and ARS staining on osteogenesis of ADSCs treated with different concentrations of FB23-2. **H** ALP activity and ARS staining quantification of ADSCs treated with different concentrations of meclofenamate sodium. Data are presented as mean ± SD by one-way ANOVA test, ns: statistically non-significant, $^{*}p < 0.05$, and $^{***}p < 0.001$ ($n = 3$ biological replicates). **I** ALP activity and ARS staining quantification of ADSCs treated with different concentrations of FB23-2. Data are presented as mean ± SD by one-way ANOVA test, ns: statistically non-significant, $^{*}p < 0.05$, $^{**}p < 0.01$, and $^{***}p < 0.001$ ($n = 3$ biological replicates). **J** Protein levels of FTO, FOXO1, RUNX2, and PPARG were determined by Western blotting analysis in the control and FB23-2 groups. Fig. S4D presents the full-length blots/gels. Data are presented as mean ± SD by two-way ANOVA test, $^{*}p < 0.05$, $^{**}p < 0.01$, $^{***}p < 0.001$ ($n = 3$ biological replicates). **K** Half-life of FOXO1 mRNA levels in ADSCs treated with FB23-2. Data are presented as mean ± SD by two-way ANOVA test and linear regression, $^{*}p < 0.05$ ($n = 3$ biological replicates). **L** Detected FOXO1 mRNA level in the IgG, FB23-2, and FB23-2 with FTO knockdown groups by RIP-qPCR. Data are presented as mean ± SD by one-way ANOVA test, $^{***}p < 0.001$ ($n = 3$ biological replicates)

molecular docking software to simulate ligand–receptor binding and observed that both meclofenamate sodium and FB23-2 could bind to the relative amino acids on the FTO enzyme (Fig. 6B and D). The binding energy of meclofenamate sodium with FTO was − 6.8 kcal/mol, while the binding energy of FB23-2 with FTO was − 8.7 kcal/mol, which suggested that FB23-2 had higher selectivity and binding ability for FTO. To determine whether meclofenamate sodium and FB23-2 could affect the osteogenic differentiation of ADSCs, the CCK-8 assay indicated that after 72 h of interaction with ADSCs, the half-maximal inhibitory concentration (IC_{50}) of meclofenamate sodium and FB23-2 were 12.23 and 8.83 μM, respectively (Fig. 6E).

We designed a concentration gradient based on the corresponding IC_{50} and added different drug concentrations into the osteogenic differentiation medium during the osteogenic induction of ADSCs. Staining, including ALP and ARS, revealed that meclofenamate sodium inhibited osteogenic differentiation of ADSCs with increasing concentration, and the visible inhibitory effect was observed at 10 μM (Fig. 6F). The quantification of ALP and ARS staining indicated that the inhibitory effect of meclofenamate sodium appeared at 8 and 10 μM, respectively (Fig. 6H). However, FB23-2 elicited a more visible inhibitory effect. Additionally, FB23-2 markedly inhibited the osteogenic effect of ADSCs under the microscope at 4 μM (Fig. 6G). The quantitative analysis of ALP and ARS staining suggested that FB23-2 exhibited the inhibitory effect at 2 μM, which was enhanced as the concentration increased (Fig. 6I). Overall, FB23-2 exhibited a greater inhibitory effect on ADSC's osteogenesis than meclofenamate sodium. Western blotting proved that 4 μM FB23-2 could inhibit FTO expression and regulate the osteogenic differentiation of ADSCs through the FTO–FOXO1 axis (Fig. 6J). In the FB23-2 group, the half-life of FOXO1 mRNA was markedly decreased, suggesting that FB23-2 inhibited osteogenic differentiation of ADSCs by reducing FOXO1 mRNA stability (Fig. 6K). Similarly, RIP-qPCR indicated that FB23-2 administration during the osteogenic differentiation could inhibit FTO and thereby reduce FOXO1 mRNA expression (Fig. 6L) and hinder osteogenesis.

FB23-2 inhibited ADSC-mediated bone formation *in vivo*

Preliminary findings established that FB23-2 inhibited osteogenic differentiation of ADSCs through FTO in vitro. To determine whether FB23-2 could inhibit the bone formation of ADSCs in vivo, we chose HA/TCP powder as ADSC's scaffold. Since the HA/TCP powder could not induce osteogenesis beneath the skin, it was mixed with ADSCs and subcutaneously implanted in the dorsal region of the nude mice for ectopic osteogenesis (Fig. 7A). Daily intraperitoneal injection of 2 mg/kg FB23-2 administered to mice could effectively inhibit FTO activity in vivo with a favorable pharmacokinetic profile [22]. In this study, mice in the FB23-2 group (ADSCs + HA/TCP + FB23-2) were administered daily intraperitoneal injections of FB23-2 at 2 mg/kg. After 8 weeks, the volume of subcutaneous bone tissue in the FB23-2 group was substantially smaller than that in the control group (ADSCs + HA/TCP) (Fig. S2F). Furthermore, the mice in the FB23-2 group did not exhibit weight loss, physical damage, or other abnormalities. The implants were harvested from the subcutaneous tissue of mice, and the images were reconstructed and analyzed using a micro-CT scanner and CTvox software. Since the subcutaneous ectopic bone tissue lacks the trabecular, BV was selected as the analysis parameter in this study. Under the micro-CT scanning, the volume of subcutaneous bone tissue in the FB23-2 group was considerably smaller than that in the control group (Fig. 7B, C). The immunohistochemical staining indicated that FTO and FOXO1 expression in the bone tissue of the control group was markedly higher than that of the FB32-2 group (Fig. 7D, E). Overall, FB23-2 could effectively inhibit bone tissue formation mediated by ADSCs in vivo.

Discussion

Epigenetic markers are regulators of MSCs' self-renewal, differentiation, and in vivo function. Epigenetic marks in MSCs can be expanded through self-renewal divisions and passed to offspring, further maintaining tissue differentiation and pathological diseases [23]. FTO belongs to the non-heme FeII/α-k dependent dioxygenase AlkB family protein, also known as ALKBH9 [24]. FTO maintained bone mass and increased mRNA stability, thereby protecting osteoblasts from genotoxic damage; however, the lack of FTO enzyme activity could drastically reduce mineral density and content in the bone tissue [25, 26]. Similarly, FOXOs are crucial for bone development, remodeling, and homeostasis in both physiological and pathological conditions. Almost all bone cells express FOXO1, 3, and 4. FOXO1 serves as the early precursors of osteoblasts [27]. In a previous study of mouse embryo models, silencing FOXO1 impacted bone formation and craniofacial development [16]. FOXO1 plays a bidirectional regulatory role in the complex process of MSCs' osteogenesis. In a diabetic fracture model, silencing FOXO1 prevented TNFα-induced BMSC apoptosis and reduced proliferation by regulating apoptotic and cell cycle genes [28]. Conversely, phytic acid resulted in circEIF4B upregulation, which triggered osteogenesis in BMSCs by promoting FOXO1, thus treating high glucose-mediated osteogenic dysfunction [29]. The previous studies reached different conclusions on the subcellular location of FTO and FOXO1. Jia et al. revealed that FTO partially colocalized with nuclear speckles and catalyzed

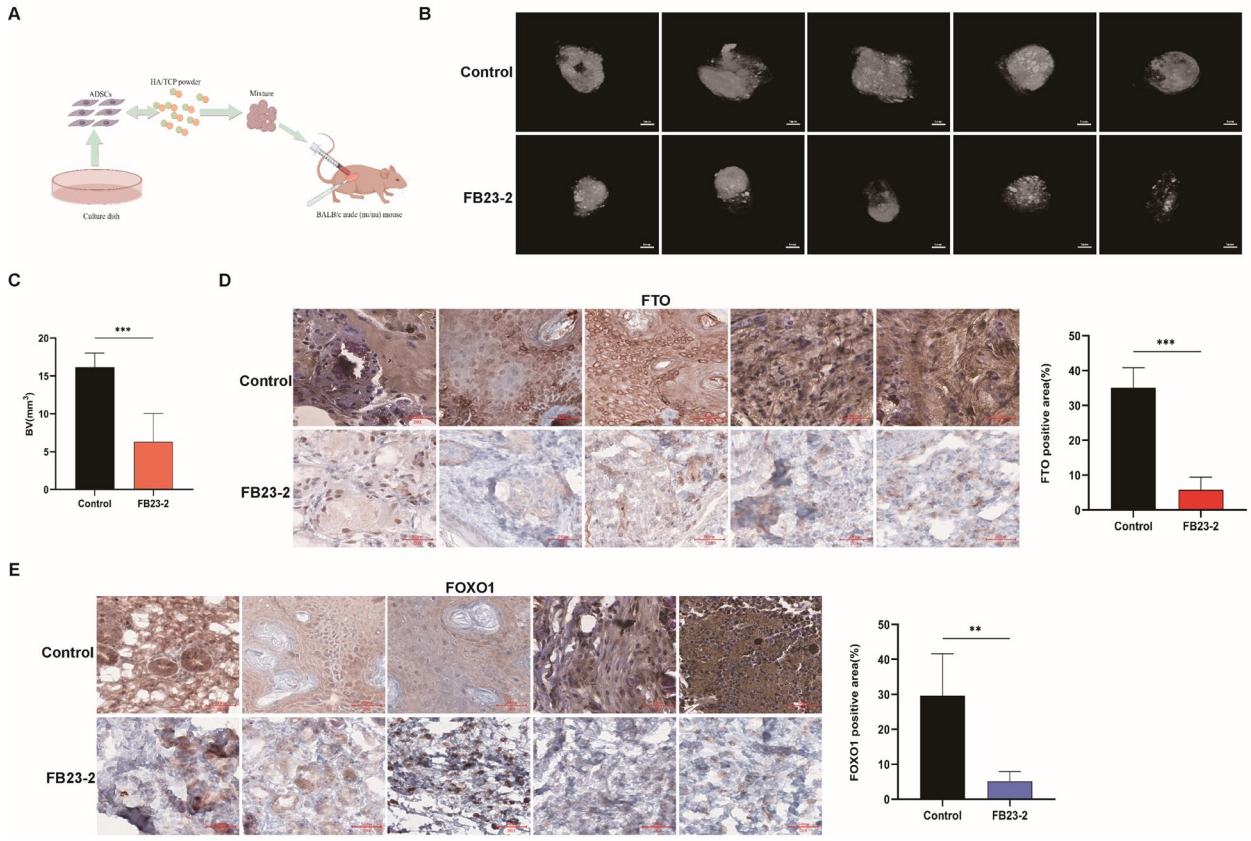

Fig. 7 FB23-2 inhibits the osteogenic differentiation of ADSCs in vivo. **A** Schematic diagram of heterotopic bone formation. **B** The micro-CT images of implantations in control and FB23-2 groups. **C** Bone tissue volume analysis of implantations by CTvox. Data are presented as mean ± SD by an unpaired *t*-test, ***$p < 0.001$ ($n = 5$). **D** Images of FTO immunostaining in bone tissues and quantitative analysis to determine the FTO protein-positive area. Data are presented as mean ± SD by an unpaired *t*-test, ***$p < 0.001$ ($n = 5$). **E** Images of FOXO1 immunostaining in bone tissues and quantitative analysis to determine the FOXO1 protein-positive area. Data are presented as mean ± SD by an unpaired *t*-test, **$p < 0.01$ ($n = 5$)

m6A demethylation of nuclear RNA [24]. However, Wei et al. suggested that FTO, in addition to targeting nuclear m6A, is located in the cytoplasm, where it facilitates the demethylation of mRNA m6A and m6Am, as well as tRNA m1A [30]. Thus, FOXO1 could shuttle between the cytoplasm and nucleus. For example, p53 directly stimulated expression of the NAD(+)-dependent histone deacetylase SIRT6, which interacted with FOXO1 and caused its deacetylation and export to the cytoplasm [31]. MST1 induced FOXO1 phosphorylation at Ser212 and translocated it to the nucleus [32]. We demonstrated for the first time that during the osteogenic differentiation of ADSCs, FTO transferred from the nucleus to the cytoplasm and bound to FOXO1 at the 1760th bp site.

During osteogenic differentiation of BMSCs, FTO mediated the demethylation of PPARG mRNA, leading to the downregulation of PPARG expression [33, 34]. Additionally, upregulated FTO promoted RUNX2 expression [35], although no study has reported their direct interaction. As previously stated, interactions between FOXO1 and RUNX2/PPARG have been reported in other cell models and biological processes. However, their regulatory relationship during MSC osteogenic differentiation remains unverified. Our study established the role of the FTO–FOXO1–RUNX2/PPARG axis in the osteogenic differentiation of ADSCs. When FTO and overexpressed FOXO1 were knocked down, the osteogenic differentiation was partially rescued. This indicated that the regulatory effect of FOXO1 on PPARG is greater than that of FTO, and there may be other pathways FTO regulates ADSC's osteogenesis, which requires further investigation.

PPARG is a ligand-dependent transcription factor that is highly expressed in adipose tissue and represents a key factor in adipogenesis and regulation [36]. Mice without PPARG exhibited increased bone mass and decreased bone marrow fat [37]. Numerous studies demonstrated that inhibiting PPARG considerably enhances the osteogenic differentiation capacity of osteoblasts or MSCs [38, 39]. Consequently, it is widely accepted that osteogenic and adipogenic differentiation often follow separate pathways, and differentiation along one lineage typically prevents the other. Wang et al. discovered that bone regeneration is a highly complex and time-coordinated

process, including stages of inflammation, cellular ingress and proliferation, angiogenesis, differentiation, and bone remodeling. PPARG knockdown disrupted bone regeneration at any stage and attenuated osteogenesis [40]. Moreover, osteogenic differentiation media for MSCs typically contain trace amounts of dexamethasone. Della et al. observed that dexamethasone did not directly upregulate RUNX2 to promote osteogenic differentiation but substantially stimulated PPARG expression in the early stages (within 7 days), leading to intracellular lipid droplet formation [41]. This suggests an alternative explanation for the observed increase in PPARG during our study's early phase. Baroi et al. reported that PPARG was highly expressed in bone cells, where it regulated cellular fuel utilization, whereas its deficiency resulted in mitochondrial dysfunction. PPARG also protected against oxidative stress and reactive oxidative species accumulation [42]. Furthermore, fatty acids can activate PPARG, promoting lipid droplet formation and fatty acid oxidation. The elevated fatty acid oxidation enhanced the osteogenesis by generating BMP7 and activating the NAD+/SIRT1/EZH2 axis [43]. Therefore, during the early stages of osteogenic differentiation, PPARG could act as an energy regulator to support bone formation. In this study, we observed that PPARG expression in the early osteogenic stage of ADSCs increased but later decreased. After FOXO1 knockdown, PPARG expression continuously increased, suggesting that adipogenic and osteogenic factors were not opposite in the early osteogenic differentiation stage of ADSCs. Hence, the PPARG role in bone formation remains controversial and requires further research.

Meclofenamic acid, a non-steroidal anti-inflammatory drug (NSAID), is known mainly for inhibiting cyclooxygenase and lipoxygenase synthesis. It is also a highly selective FTO inhibitor that competes with FTO by binding with the m6A-containing nucleic acid to suppress its expression [44]. Meclofenamate sodium replaces the -OH with the -ONA group based on meclofenamic acid. It has better solubility and stability than meclofenamic acid. Meclofenamate sodium is approved for arthritis, pain relief, and dysmenorrhea [45, 46]. Huang et al. developed FB23 and FB23-2 based on retaining the key element of meclofenamic acid, benzylcarboxylic acid [22]. These two

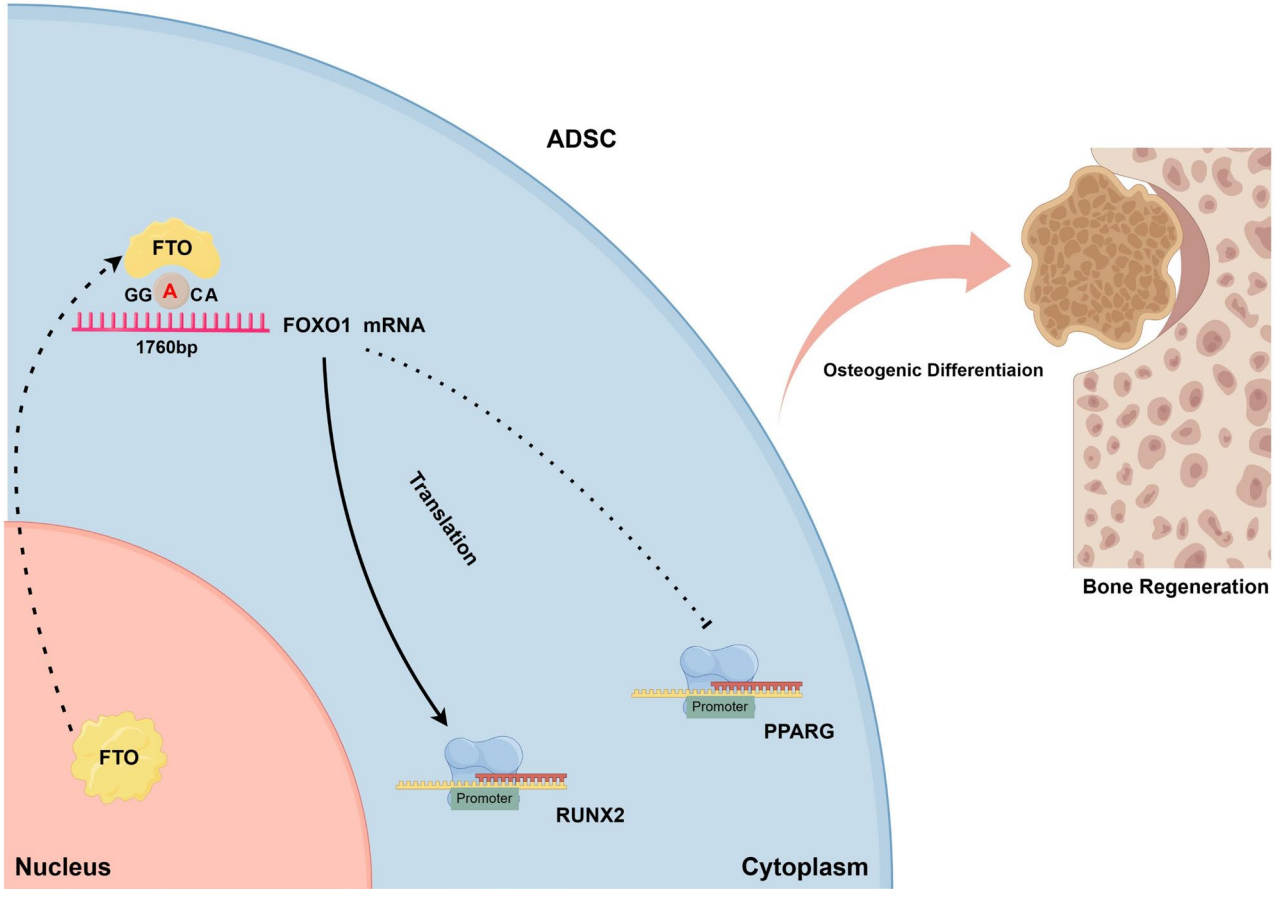

Fig. 8 Working model depicting FTO–FOXO1–RUNX2/PPARG axis in the osteogenic differentiation of ADSCs. FTO translocated to the cytoplasm and bound FOXO1 mRNA to enhance its expression during ADSC's osteogenesis. FOXO1 activated RUNX2 and repressed PPARG via promoter binding, ultimately regulating osteogenic differentiation

small-molecule inhibitors were more selective for FTO. Neither of them inhibited the demethylation of ALKBH5; however, FB23-2 had better cell permeability than FB23. We revealed the optimal concentration of meclofenamate sodium and FB23-2 to inhibit osteogenic differentiation in ADSCs in vitro for the first time. Compared with meclofenamate sodium, FB23-2 elicited a pronounced inhibitory effect on osteogenic differentiation. Meanwhile, FB23-2 impaired the proliferation and osteogenic differentiation of ADSCs by inhibiting the FTO–FOXO1 axis in vitro and in vivo. Mefenamic acid is commonly utilized in clinical settings, characterized by its rapid absorption following oral administration and a relatively short half-life, making it more tolerable than many other NSAIDs [47]. This suggests that as the application of ADSCs in the field of bone reconstruction gradually increases, some patients may experience pain alongside their bone defects [48]. Consequently, the long-term use of analgesics containing FTO inhibitors should be carefully evaluated.

In summary, our study elucidated specific mechanisms of m6A modification in ADSC-mediated bone regeneration. Specifically, FTO promoted RUNX2 expression while inhibiting PPARG expression by binding to m6A modification sites on FOXO1, thus jointly regulating the proliferation and osteogenic differentiation (Fig. 8). The NSAIDs commonly used in clinical practice inhibit FTO, which can impact ADSC-mediated bone regeneration through the aforementioned pathway. As ADSCs are increasingly utilized in bone tissue engineering, our study advances the current knowledge on the impact of m6A modification in regulating osteogenic differentiation of ADSCs. This insight can potentially lead to innovative treatment approaches and drug applications for individuals with bone defects utilizing ADSCs.

Supplementary Information

The online version contains supplementary material available at https://doi.org/10.1186/s13287-025-04862-w.

Supplementary Material 1

Supplementary Material 2

Supplementary Material 3

Supplementary Material 4

Artificial intelligence (AI)

The authors declare that they have not used AI-generated work in this manuscript.

Author contributions

Zhaohua Wang, Shu Guo and Shude Yang contributed to this review conception and direction. Zhaohua Wang and Si Wen performed the experiments. Huizheng Li and Xiaosu Wang collected reasonably related literature materials. Zhaohua Wang designed and drew figures. Zhaohua Wang drafted the manuscript. Shu Guo and Shude Yang revised the manuscript critically. All authors approved the final manuscript.

Funding

This work was sponsored by the National Natural Science Foundation of China (51872332, 82301045).

Data availability

No datasets were generated or analysed during the current study.

Declarations

Ethics approval and consent to participate

1. The study entitled "Exosomes regulate the osteogenic efficacy and mechanism of ADSCS in Col I-RGD modified n-HAP scaffold Research" was approved by the Ethics Committee of the First Hospital of China Medical University (Date: Feb 26, 2018, [2018]2018-110-2). The original source confirmed that the collection of ADSCs received initial ethical approval and the donor signed an informed consent form. 2. All animal experiments conducted in this study were approved by the Laboratory Animal Welfare and Ethical Review of China Medical University under the title "The Application and Research of Adipose-Derived Stem Cells" with authorization number CMU20231074, first approved on October 20, 2023. All procedures were carried out in accordance with the China Medical University Animal Experimentation Regulations. Throughout the experimental period, the health status of the mice was monitored by observing their activity levels, general behavior, and weight conditions. Other than surgical intervention, no humane endpoints were set, as the protocol posed no risk of distress.

Competing interests

The authors declare no competing interests.

Received: 12 July 2025 / Accepted: 8 December 2025
Published online: 17 December 2025

References

1. Zhao ZH, Ma XL, Zhao B, Tian P, Ma JX, Kang JY, et al. Naringin-inlaid silk fibroin/hydroxyapatite scaffold enhances human umbilical cord-derived mesenchymal stem cell-based bone regeneration. Cell Prolif. 2021;54(7):e13043.
2. Kazimierczak P, Przekora A. Bioengineered living bone grafts-a concise review on bioreactors and production techniques in vitro. Int J Mol Sci. 2022. https://doi.org/10.3390/ijms23031765.
3. Zhou T, Yuan Z, Weng J, Pei D, Du X, He C, et al. Challenges and advances in clinical applications of mesenchymal stromal cells. J Hematol Oncol. 2021;14(1):24.
4. Pittenger MF, Mackay AM, Beck SC, Jaiswal RK, Douglas R, Mosca JD, et al. Multilineage potential of adult human mesenchymal stem cells. Science. 1999;284(5411):143–7.
5. Yoshida Y, Matsubara H, Fang X, Hayashi K, Nomura I, Ugaji S, et al. Adipose-derived stem cell sheets accelerate bone healing in rat femoral defects. PLoS One. 2019;14(3):e0214488.
6. Ciuffi S, Zonefrati R, Brandi ML. Adipose stem cells for bone tissue repair. Clin Cases Miner Bone Metab. 2017;14(2):217–26.
7. Klemm SL, Shipony Z, Greenleaf WJ. Chromatin accessibility and the regulatory epigenome. Nat Rev Genet. 2019;20(4):207–20.
8. Walewska A, Janucik A, Tynecka M, Moniuszko M, Eljaszewicz A. Mesenchymal stem cells under epigenetic control - the role of epigenetic machinery in fate decision and functional properties. Cell Death Dis. 2023;14(11):720.
9. Ries RJ, Zaccara S, Klein P, Olarerin-George A, Namkoong S, Pickering BF, et al. M(6)A enhances the phase separation potential of mRNA. Nature. 2019;571(7765):424–8.
10. Zheng HX, Zhang XS, Sui N. Advances in the profiling of N(6)-methyladenosine (m(6)A) modifications. Biotechnol Adv. 2020;45:107656.
11. Batista PJ, Molinie B, Wang J, Qu K, Zhang J, Li L, et al. m(6)A RNA modification controls cell fate transition in mammalian embryonic stem cells. Cell Stem Cell. 2014;15(6):707–19.
12. Chen X, Zhao Q, Zhao YL, Chai GS, Cheng W, Zhao Z, et al. Targeted RNA N(6) -methyladenosine demethylation controls cell fate transition in human pluripotent stem cells. Adv Sci. 2021;8(11):e2003902.

13. Wang Z, Wen S, Zhong M, Yang Z, Xiong W, Zhang K, et al. Epigenetics: novel crucial approach for osteogenesis of mesenchymal stem cells. J Tissue Eng. 2023;14:20417314231175364.
14. Sun W, Song Y, Xia K, Yu L, Huang X, Zhao Z, et al. Transcriptome-wide m(6) A methylome during osteogenic differentiation of human adipose-derived stem cells. Stem Cell Res Ther. 2021;12(1):489.
15. Fan W, Imamura T, Sonoda N, Sears DD, Patsouris D, Kim JJ, et al. FOXO1 transrepresses peroxisome proliferator-activated receptor gamma transactivation, coordinating an insulin-induced feed-forward response in adipocytes. J Biol Chem. 2009;284(18):12188–97.
16. Teixeira CC, Liu Y, Thant LM, Pang J, Palmer G, Alikhani M. Foxo1, a novel regulator of osteoblast differentiation and skeletogenesis. J Biol Chem. 2010;285(40):31055–65.
17. Xiao Y, Wang Y, Tang Q, Wei L, Zhang X, Jia G. An elongation- and ligation-based qPCR amplification method for the radiolabeling-free detection of locus-specific N(6) -methyladenosine modification. Angew Chem Int Ed Engl. 2018;57(49):15995–6000.
18. Zhang H, Shi X, Huang T, Zhao X, Chen W, Gu N, et al. Dynamic landscape and evolution of m6A methylation in human. Nucleic Acids Res. 2020;48(11):6251–64.
19. Jiang X, Liu B, Nie Z, Duan L, Xiong Q, Jin Z, et al. The role of m6A modification in the biological functions and diseases. Signal Transduct Target Ther. 2021;6(1):74.
20. Yue SW, Liu HL, Su HF, Luo C, Liang HF, Zhang BX, et al. M6A-regulated tumor glycolysis: new advances in epigenetics and metabolism. Mol Cancer. 2023;22(1):137.
21. Mende W, Götzl R, Kubo Y, Pufe T, Ruhl T, Beier JP. The role of adipose stem cells in bone regeneration and bone tissue engineering. Cells. 2021. https://doi.org/10.3390/cells10050975.
22. Huang Y, Su R, Sheng Y, Dong L, Dong Z, Xu H, et al. Small-Molecule targeting of oncogenic FTO demethylase in acute myeloid leukemia. Cancer Cell. 2019;35(4):677–e9110.
23. Sui BD, Zheng CX, Li M, Jin Y, Hu CH. Epigenetic regulation of mesenchymal stem cell homeostasis. Trends Cell Biol. 2020;30(2):97–116.
24. Jia G, Fu Y, Zhao X, Dai Q, Zheng G, Yang Y, et al. N6-methyladenosine in nuclear RNA is a major substrate of the obesity-associated FTO. Nat Chem Biol. 2011;7(12):885–7.
25. Sachse G, Church C, Stewart M, Cater H, Teboul L, Cox RD, et al. FTO demethylase activity is essential for normal bone growth and bone mineralization in mice. Biochimica et Biophysica Acta (BBA). 2018;1864(3):843–50.
26. Zhang Q, Riddle RC, Yang Q, Rosen CR, Guttridge DC, Dirckx N, et al. The RNA demethylase FTO is required for maintenance of bone mass and functions to protect osteoblasts from genotoxic damage. Proc Natl Acad Sci U S A. 2019;116(36):17980–9.
27. Ma X, Su P, Yin C, Lin X, Wang X, Gao Y, et al. The roles of FoxO transcription factors in regulation of bone cells function. Int J Mol Sci. 2020. https://doi.org/10.3390/ijms21030692.
28. Ko KI, Coimbra LS, Tian C, Alblowi J, Kayal RA, Einhorn TA, et al. Diabetes reduces mesenchymal stem cells in fracture healing through a TNFα-mediated mechanism. Diabetologia. 2015;58(3):633–42.
29. Wu J, Li X, Nie H, Shen Y, Guo Z, Huihan Chu C, et al. Phytic acid promotes high glucose-mediated bone marrow mesenchymal stem cells osteogenesis via modulating circEIF4B that sponges miR-186-5p and complexes with IGF2BP3. Biochem Pharmacol. 2024;222:116118.
30. Wei J, Liu F, Lu Z, Fei Q, Ai Y, He PC, et al. Differential m(6)A, m(6)A(m), and m(1)A demethylation mediated by FTO in the cell nucleus and cytoplasm. Mol Cell. 2018;71(6):973–e855.
31. Zhang P, Tu B, Wang H, Cao Z, Tang M, Zhang C, et al. Tumor suppressor p53 cooperates with SIRT6 to regulate gluconeogenesis by promoting FoxO1 nuclear exclusion. Proc Natl Acad Sci U S A. 2014;111(29):10684–9.
32. Yuan Z, Lehtinen MK, Merlo P, Villén J, Gygi S, Bonni A. Regulation of neuronal cell death by MST1-FOXO1 signaling. J Biol Chem. 2009;284(17):11285–92.
33. Chen LS, Zhang M, Chen P, Xiong XF, Liu PQ, Wang HB, et al. The m(6)A demethylase FTO promotes the osteogenesis of mesenchymal stem cells by downregulating PPARG. Acta Pharmacol Sin. 2021. https://doi.org/10.1038/s41401-021-00756-8.
34. Shen GS, Zhou HB, Zhang H, Chen B, Liu ZP, Yuan Y, et al. The GDF11-FTO-PPARγ axis controls the shift of osteoporotic MSC fate to adipocyte and inhibits bone formation during osteoporosis. Biochimica et Biophysica Acta (BBA). 2018;1864(12):3644–54.
35. Zhang X, Wang Y, Zhao H, Han X, Zhao T, Qu P, et al. Extracellular vesicle-encapsulated miR-22-3p from bone marrow mesenchymal stem cell promotes osteogenic differentiation via FTO inhibition. Stem Cell Res Ther. 2020;11(1):227.
36. Ma X, Wang D, Zhao W, Xu L. Deciphering the roles of PPARγ in adipocytes via dynamic change of transcription complex. Front Endocrinol (Lausanne). 2018;9:473.
37. Baroi S, Czernik PJ, Chougule A, Griffin PR, Lecka-Czernik B. PPARG in osteocytes controls sclerostin expression, bone mass, marrow adiposity and mediates TZD-induced bone loss. Bone. 2021;147:115913.
38. Sun H, Kim JK, Mortensen R, Mutyaba LP, Hankenson KD, Krebsbach PH. Osteoblast-targeted suppression of PPARγ increases osteogenesis through activation of mTOR signaling. Stem Cells. 2013;31(10):2183–92.
39. Takada I, Kouzmenko AP, Kato S. Wnt and PPARgamma signaling in osteoblastogenesis and adipogenesis. Nat Rev Rheumatol. 2009;5(8):442–7.
40. Wang C, Tanjaya J, Shen J, Lee S, Bisht B, Pan HC, et al. Peroxisome proliferator-activated receptor-γ knockdown impairs bone morphogenetic protein-2-induced critical-size bone defect repair. Am J Pathol. 2019;189(3):648–64.
41. Della Bella E, Buetti-Dinh A, Licandro G, Ahmad P, Basoli V, Alini M, et al. Dexamethasone induces changes in osteogenic differentiation of human mesenchymal stromal cells via SOX9 and PPARG, but not RUNX2. Int J Mol Sci. 2021. https://doi.org/10.3390/ijms22094785.
42. Baroi S, Czernik PJ, Khan MP, Letson J, Crowe E, Chougule A, et al. PPARG in osteocytes controls cell bioenergetics and systemic energy metabolism independently of sclerostin levels in circulation. Mol Metab. 2024;88:102000.
43. Zheng ZY, Jiang T, Huang ZF, Chu B, Gu J, Zhao X, et al. Fatty acids derived from apoptotic chondrocytes fuel macrophages FAO through MSR1 for facilitating BMSCs osteogenic differentiation. Redox Biol. 2022;53:102326.
44. Huang Y, Yan J, Li Q, Li J, Gong S, Zhou H, et al. Meclofenamic acid selectively inhibits FTO demethylation of m6A over ALKBH5. Nucleic Acids Res. 2015;43(1):373–84.
45. Ghosh R, Hwang SM, Cui Z, Gilda JE, Gomes AV. Different effects of the nonsteroidal anti-inflammatory drugs meclofenamate sodium and Naproxen sodium on proteasome activity in cardiac cells. J Mol Cell Cardiol. 2016;94:131–44.
46. Vargyas JM, Campeau JD, Mishell DR Jr. Treatment of menorrhagia with meclofenamate sodium. Am J Obstet Gynecol. 1987;157(4 Pt 1):944–50.
47. Lago EM, Silva MP, Queiroz TG, Mazloum SF, Rodrigues VC, Carnaúba PU, et al. Phenotypic screening of nonsteroidal anti-inflammatory drugs identified mefenamic acid as a drug for the treatment of schistosomiasis. EBioMedicine. 2019;43:370–9.
48. Goodman SB, Lin T. Modifying MSC phenotype to facilitate bone healing: biological approaches. Front Bioeng Biotechnol. 2020;8:641.

Publisher's Note